Minimally-constrained flight simulation in a wind tunnel

Punsara D. B. Navaratna* , Mark H. Lowenberg † and Simon A. Neild ‡
Department of Aerospace Engineering, University of Bristol, Bristol, BS8 1TR, United Kingdom

Experimental studies into aircraft stability and performance can be enhanced by using a rig in which the aircraft model support approximates free flight within a wind tunnel. Such multi-degree-of-freedom wind tunnel rigs often impose kinematic restrictions on the aircraft model's translational motion. This study investigates these kinematic effects, with particular attention to a spherical constraint where the aircraft is held at the end of a fixed length pivoting arm. Here the motions of the aircraft and kinematic constraints are derived as differential-algebraic equations and assessed numerically. The impact is found mainly on translational motion with negligible effect on the aircraft's rotation. A concept to reduce these kinematic effects on the aircraft's motion by applying an external force onto the aircraft is proposed. This compensation, which partially accounts for the constraints on the aircraft motion, is shown to reduce the effects of the arm, allowing for improved physical simulation.

Nomenclature

α	Angle of attack
β	Angle of sideslip
$\ddot{\boldsymbol{\theta}}$	Vector of rotational accelerations
$\ddot{\boldsymbol{q}}$	Linear and rotational accelerations vector
$\ddot{\boldsymbol{R}}$	Vector of linear accelerations
$\boldsymbol{\lambda}$	Lagrange multiplier
$\overline{\boldsymbol{F}}_{\boldsymbol{\theta}}$	Vector of external moments
$\boldsymbol{Q_C}$	Virtual constraint force
$\boldsymbol{Q_E}$	External forces and moments vector
$\overline{\boldsymbol{\omega}}$	Aircraft body axes rotational velocity vector

*PhD Student.
†Professor of Flight Dynamics, AIAA Senior Member.
‡Professor of Nonlinear Structural Dynamics.

$\boldsymbol{\theta_q}$ Quaternions vector representing rotation

$\boldsymbol{Q_R}$ Vector of external forces

$\ddot{x}$, $\ddot{y}$, $\ddot{z}$ Inertial axes linear accelerations

δ_a, δ_e, δ_r Aileron, elevator and rudder deflections

$\dot{\overline{p}}$, $\dot{\overline{q}}$, $\dot{\overline{r}}$ Body axes rotational accelerations

$\hat{\mathbf{p}}$ Normalized position vector of the aircraft model relative to the center of the spherical constraint

$\mathbf{a_{cen}}$ Centripetal acceleration vector of the aircraft model

$\mathbf{a_{tan}}$ Tangential acceleration vector of the aircraft model

$\mathbf{a}$ Total acceleration vector of the aircraft model

$\mathbf{F_{tan}}$ Resultant tangential force acting on the aircraft model

$\mathbf{F_{yz}}$ Projected total aerodynamic and inertial force on the yz plane

ω Angular velocity of the aircraft about the spherical constraint

$\overline{G}$ Quaternion transformation matrix

$\overline{I}_{ab}$ Aircraft inertia about axis ab

$\overline{M}_x$, $\overline{M}_y$, $\overline{M}_z$ Body axes moments

ϕ, θ, ψ Aircraft roll, pitch, and yaw attitudes

ρ Air density

θ_s, ϕ_s Spherical coordinates: inclination and azimuth angles

b Reference wing span

c Reference aerodynamic chord

C_D Non-dimensional coefficients for drag

C_L Non-dimensional coefficients for lift

C_l Non-dimensional coefficients for rolling moment

C_m Non-dimensional coefficients for pitching moment

C_n Non-dimensional coefficients for yawing moment

C_q Constraint Jacobian matrix

C_Y Non-dimensional coefficients for side force

F_c Externally applied tangential force compensating for spherical constraint effects

F_x, F_y, F_z Inertial axes forces

L, D, Y Lift, drag, and side force

l, m, n Rolling, pitching, and yawing moments

M Mass and inertia tensor matrix

m_a Aircraft mass

m_{RR} Mass matrix

p, q, r Body axes roll, pitch, and yaw rates

r Spherical constraint radius

R_{rad} Radial reaction force between the aircraft model and spherical constraint

S Reference wing area

V Wind speed

X, Y, Z Forces in the inertial frame of reference

x, y, z Translations in the inertial frame of reference

$\overline{I}_{\theta\theta}$ Inertia tensor matrix

I. Introduction

Investigations of aircraft stability, controllability, and upset behavior (including assessment of handling qualities and control law performance) have been conducted using sub-scale free-flying models inside a wind tunnel or by full-scale flight tests [1]. A potential alternative method, or perhaps intermediate stage, for achieving the same objective could be provided by an experimental rig capable of approximately simulating free-flight conditions within a wind tunnel. A configuration of this typeallows the testing of more conventional models – models which do not have the capability of generating thrust. However, these rigs inherently apply physical constraints on the aircraft model, limiting its overall motion depending on the degrees-of-freedom (DOF) available. Examples of such rigs are the 3-DOF traverse rig at the Georgia Institute of Technology [2], the 3-DOF Dynamic Plunge-Pitch-Roll rig (DyPPiR) at the Virginia Polytechnic Institute and State University [3] and the 5-DOF maneuver rig at the University of Bristol [4]. There also exist full 6-DOF rigs in which these constraints are not imposed, such as the Stuart platform or the Model Positioning Mechanism, which are based on the parallel kinematic concept [5]. However, these rigs typically have a limited working space, reduced stiffness at some locations of the workspace in a certain direction, and the rig itself can be large in size.

Experimental rigs such as the 5-DOF maneuver rig have previously been used to study nonlinear and time-dependant aerodynamic effects, as well as for the development of mathematical models via parameter estimation and aerodynamic characterization of model aircraft [6, 7, 8, 9, 10]. Here, we investigate the effect of the kinematic constraints on the aircraft model dynamics. For example, a change in lift, drag or side force on a model supported on a freely rotating rig arm will induce a rotation – rather than a pure translation – of the trajectory of the model center of gravity. Similarly, aerodynamic and inertial loads on the moving parts of the rig itself will contribute further to the rig-induced kinematics. The resulting changes in motion relative to the same model without constraints in turn affects the variations in loads. Hence the model and

rig dynamics are coupled and the purpose of this study is to understand where this coupling is strongest, the consequences thereof and how the effects of this coupling may be reduced.

The latter possibility arises if the rig is able to generate additional forces in response to the coupled dynamics: this offers the opportunity to reduce the influence of the kinematic constraints on the aircraft maneuvers performed by applying a force in line with that constraint (e.g. a tangential force for a spherical constraint). Here, the system equations of motion are analyzed by constructing algebraic and differential equations, to describe both the unconstrained and constrained aircraft dynamics.

The suitability of performing aircraft model maneuvers while constrained by the experimental rig is assessed by comparing them with those from an unconstrained aircraft model producing its own thrust. The comparison is done by assessing the responses in longitudinal and lateral-directional modes. Each of these modes is excited individually by giving specific control surface inputs. Note: thrust must always be present for the unconstrained aircraft whereas it is not necessary but can be beneficial for the constrained aircraft. Thrust is retained for initial comparisons of constrained versus unconstrained motions so any observed changes are purely due to the imposed constraints. Then the usual constrained no-thrust aircraft model will be considered. The differences in responses are compared quantitatively using the root mean square error of the relative distance, attitude and angular rates between the unconstrained and constrained aircraft. In addition, the level of significance of the kinematic constraints on the model aerodynamics is studied by estimating the aircraft's aerodynamic coefficients using the recorded motion. The estimation is accomplished using the equation error method parameter estimation technique.

A method to reduce the difference in responses, by reducing the effects of the rig constraints on the aircraft motion, is then proposed and assessed. The method, which does not require the aircraft model to provide thrust, involves applying an external force onto the constrained aircraft through the aircraft's pivot (or rig attachment point). Achieving a minimal motion difference relative to a free-flying model will make it possible to perform physical simulation of short term maneuvers on an experimental rig for investigative purposes such as stability and response evaluation or control law development. In reality, this capability is dependent on the type of experimental rig being used. For example, the dynamic 5 degree-of-freedom maneuver rig, shown in figure 1, is capable of applying an external force onto the aircraft model using its aerodynamic compensator at the downstream end of the rig arm. Applying this force provides a means of controlling the reaction force between the experimental rig and aircraft. To provide the reaction force variation to ensure correct compensation as the aircraft model maneuvers in the tunnel (e.g. via control surface actuation) requires feedback control. In this paper, the effectiveness of an idealized reaction force control on the model motions relative to free flight is evaluated: the impact of practical implementation issues such as measurement noise and lags on the compensated model responses as well as means to reduce

them would need to follow this study. Note: the maneuver rig itself has a total of 6 degrees-of-freedom in total, however the rig only provides 5 degrees-of-freedom to the aircraft model as it does not provide fore-aft translation. The model-gimbal has an extra roll freedom essentially separating the rig and aircraft model roll inertias.The concept of reaction force feedback control is also beneficial for cases where inertial loads created by the model being tested are important such as the experimental approach to investigate a flapping wing model [11].

Section II describes the different kinematic constraints associated with various experimental rig types. Section III presents the mathematical model used for the numerical simulation, along with the aerodynamic model used. The derivations for the spherical and planar kinematic constraints are also shown. Section IV then compares the effects these constraints have on the aircraft response by exciting its various modes. Note: in this section thrust will be simulated for all aircraft, even while constrained so any differences in motion are purely due to the kinematic constraint. Section V introduces the concept of a compensation force which can be applied to the aircraft to reduce the effects of the spherical constraint on its motion, allowing for a closer match with a free-flying aircraft. Note: with this compensation approach the constrained aircraft will not be required to produce thrust, as is the case with most wind tunnel testing. Responses are compared visually with time history plots, root mean square error, as well as perceived aerodynamic coefficients found using parameter estimation. Finally section VI investigates the effects of transmission delay on the effectiveness of this compensation force before conclusions are drawn.

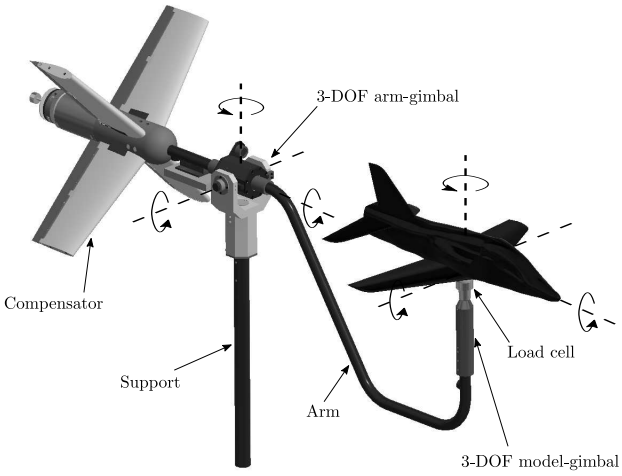

Fig. 1: The dynamic multi-DOF maneuver rig.

II. Physical kinematic constraint

Ideally wind tunnel testing of subscale aircraft models would be conducted in free flight, however this requires the model to be capable of providing thrust, along with needing accurate control algorithms. As

traditional subscale wind tunnel models do not provide thrust a rig is required to provide a longitudinal constraint to mimic flight, albeit at a constant ground velocity. However, a subscale aircraft model supported on such a dynamic test rig is inevitably subject to a limitation in its range of translational and/or rotational motion. The effect of this restriction on aircraft motion, and hence on velocity and acceleration due to aerodynamic loads depends on the experimental rig. Here we consider how it differs from the motion of an unconstrained aircraft controlled to travel close to constant ground velocity.

The traverse rig shown in figure 2 is capable of 3-DOFs: model pitch, roll, and heave [2] made possible by two translation and rotation supports on either sides of the model. For this rig, the model motion is essentially constrained to translate along a vertical line. The 3-DOF forced oscillation DyPPiR rig, see figure 3, is capable of model pitch, roll, and heave [3], similar to the traverse rig. The model is held by a sting which can rotate in pitch and roll, and translate vertically via the support system. The dynamic 5-DOF maneuver rig (shown in figure 1) is capable of aircraft roll, pitch and yaw, as well as approximate heave and sway motions with the rotation of its arm. Continuous roll has been achieved with the assistance of arm roll provided by the arm gimbal, which would otherwise be impossible due to rotation limits of the model gimbal [4]. Specifically, the maneuver rig constrains the translational motion of the aircraft to tangential motion only, due to the fixed length of its arm (0.8m between the arm gimbal and model gimbal). The model is constrained to move along an arc in two dimensions, or on a surface of a sphere in three dimensions. For small rig pitch and yaw rotations, the aircraft motion may be approximated as heave and sway respectively, however, for large rig rotations the curved motion of the aircraft does have a noticeable effect on its response [12].

Here, two physical kinematic constraints are explored: a spherical constraint (as is the case with the 5-DOF maneuver rig) and a planar constraint (similar to the 3-DOF traverse rig), as shown in figure 4.

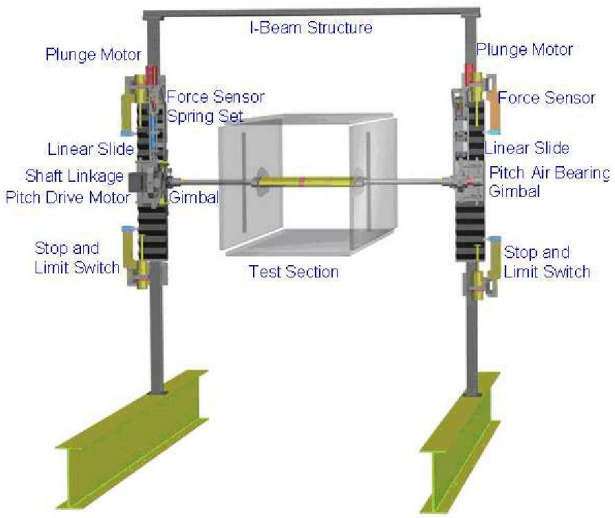

Fig. 2: The 3-DOF traverse rig [2].

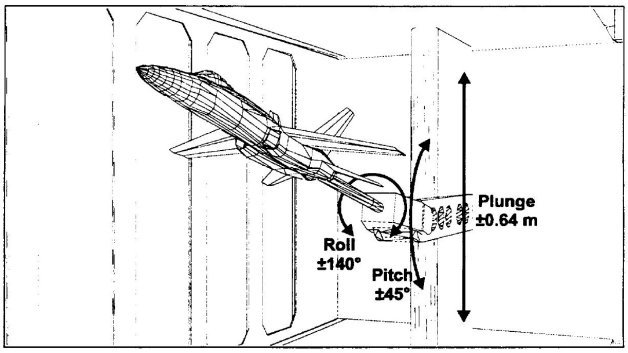

Fig. 3: The 3-DOF DyPPiR rig [3].

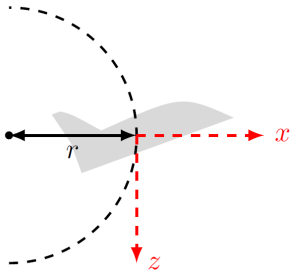

(a) Spherical constraint

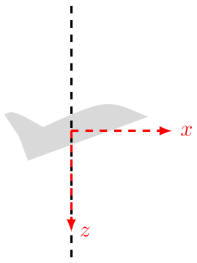

(b) Planar constraint

Fig. 4: Physical kinematic constraints

III. Mathematical model

The rigid-body equations of motion are described below in the Newton-Euler form which can be extended for multi-body systems [13]. The method uses Lagrange multipliers ($\boldsymbol{\lambda}$) to simultaneously solve the equations for single-body dynamics together with constraint equations. For an arbitrary system of bodies, the equations can be written in differential-algebraic form

$$\begin{bmatrix} M & {C_q}^T \\ C_q & 0_{nc} \end{bmatrix} \begin{bmatrix} \ddot{\boldsymbol{q}} \\ \boldsymbol{\lambda} \end{bmatrix} = \begin{bmatrix} \boldsymbol{Q_E} \\ \boldsymbol{Q_C} \end{bmatrix}. \tag{1}$$

In Eq. (1), M is the mass and inertial tensor matrix for individual bodies (where the body axis origin coincides with its center of mass), $\ddot{\boldsymbol{q}}$ is a vector of linear and rotational accelerations in the system's generalized coordinates, $\boldsymbol{Q_E}$ is the external forces and moments vector and C_q is the constraint Jacobian matrix. C_q and $\boldsymbol{Q_C}$ are derived by differentiating the constraint equations twice with respect to time (see following subsections). The subscript nc in Eq. (1) represents the number of constraint equations used. The ${C_q}^T\boldsymbol{\lambda}$

term is effectively the total reaction force acting on each body. In more detail we can write

$$M = \begin{bmatrix} M^1 & 0 & \cdots & 0 \\ 0 & M^2 & \cdots & 0 \\ \vdots & \vdots & \ddots & 0 \\ 0 & 0 & 0 & M^n \end{bmatrix}, \ddot{\boldsymbol{q}} = \begin{bmatrix} \ddot{\boldsymbol{q}}^1 \\ \ddot{\boldsymbol{q}}^2 \\ \vdots \\ \ddot{\boldsymbol{q}}^n \end{bmatrix}, \boldsymbol{Q_E} = \begin{bmatrix} \boldsymbol{Q_E^1} \\ \boldsymbol{Q_E^2} \\ \vdots \\ \boldsymbol{Q_E^n} \end{bmatrix}, \tag{2}$$

$$M^i = \begin{bmatrix} {m_{RR}}^i & 0_3 \\ 0_3 & {\overline{I}_{\theta\theta}}^i \end{bmatrix}, {m_{RR}}^i = \begin{bmatrix} m_a^i & 0 & 0 \\ 0 & m_a^i & 0 \\ 0 & 0 & m_a^i \end{bmatrix}, {\overline{I}_{\theta\theta}}^i = \begin{bmatrix} {\overline{I}_{xx}}^i & -{\overline{I}_{xy}}^i & -{\overline{I}_{xz}}^i \\ -{\overline{I}_{yx}}^i & {\overline{I}_{yy}}^i & -{\overline{I}_{yz}}^i \\ -{\overline{I}_{zx}}^i & -{\overline{I}_{zy}}^i & {\overline{I}_{zz}}^i \end{bmatrix}, \tag{3}$$

$$\ddot{\boldsymbol{q}}^i = \begin{bmatrix} \ddot{\boldsymbol{R}}^i \\ \ddot{\overline{\boldsymbol{\theta}}}^i \end{bmatrix}, \ddot{\boldsymbol{R}}^i = \begin{bmatrix} \ddot{x}^i \\ \ddot{y}^i \\ \ddot{z}^i \end{bmatrix}, \ddot{\overline{\boldsymbol{\theta}}}^i = \begin{bmatrix} \dot{\overline{p}}^i \\ \dot{\overline{q}}^i \\ \dot{\overline{r}}^i \end{bmatrix}, \tag{4}$$

$$\boldsymbol{Q_E}^{\boldsymbol{i}} = \begin{bmatrix} \boldsymbol{Q_R}^{\boldsymbol{i}} \\ \overline{\boldsymbol{F}}_{\boldsymbol{\theta}}{}^{\boldsymbol{i}} - \overline{\boldsymbol{\omega}}^{\boldsymbol{i}} \times {\overline{I}_{\theta\theta}}^i \overline{\boldsymbol{\omega}}^{\boldsymbol{i}} \end{bmatrix}, \boldsymbol{Q_R}^{\boldsymbol{i}} = \begin{bmatrix} {F_x}^i \\ {F_y}^i \\ {F_z}^i \end{bmatrix}, \overline{\boldsymbol{F}_{\boldsymbol{\theta}}}^{\boldsymbol{i}} = \begin{bmatrix} {\overline{M}_x}^i \\ {\overline{M}_y}^i \\ {\overline{M}_z}^i \end{bmatrix}, \overline{\boldsymbol{\omega}}^{\boldsymbol{i}} = \begin{bmatrix} \overline{p}^i \\ \overline{q}^i \\ \overline{r}^i \end{bmatrix}. \tag{5}$$

Here $\boldsymbol{Q_R}^{\boldsymbol{i}}$ and $\boldsymbol{F}_{\boldsymbol{\theta}}^i$ are the force and moment vectors respectively. $\boldsymbol{\omega}^{\boldsymbol{i}}$ is the body rotational velocity vector. Note: the bar above a symbol represents the quantity in the local body frame of reference. The above equations can be expanded to recreate the conventional form of the translational and rotational nonlinear single-body rigid equations of motion for an aircraft. Here, a Cartesian coordinate system is used along with quaternions to represent rotations.

The use of quaternions requires the following changes to be made to Eq. (3) to (5):

$$\boldsymbol{\theta_q}^{\boldsymbol{i}} = \begin{bmatrix} {\theta_0}^i \\ {\theta_1}^i \\ {\theta_2}^i \\ {\theta_3}^i \end{bmatrix}, \tag{6}$$

$$M^i = \begin{bmatrix} {m_{RR}}^i & 0_{3,4} \\ 0_{4,3} & {\overline{G}^i}^T {\overline{I}_{\theta\theta}}^i \overline{G}^i \end{bmatrix}, \boldsymbol{Q_E}^{\boldsymbol{i}} = \begin{bmatrix} \boldsymbol{Q_R}^{\boldsymbol{i}} \\ {\overline{G}^i}^T \left(\overline{\boldsymbol{F_\theta}}^{\boldsymbol{i}} - \overline{\boldsymbol{\omega}}^{\boldsymbol{i}} \times {\overline{I}_{\theta\theta}}^i \overline{\boldsymbol{\omega}}^{\boldsymbol{i}} \right) \end{bmatrix}, \overline{\boldsymbol{\omega}}^{\boldsymbol{i}} = \overline{G}^i \dot{\overline{\boldsymbol{\theta}}}_{\boldsymbol{q}}^{\boldsymbol{i}}, \tag{7}$$

where ${\theta_{0-3}}^i$ are the quaternion Euler parameters, and $\overline{G}^i$ is a quaternion transformation matrix (see appendix A). To begin with, only a single body (the aircraft) will be examined so the superscript i is removed for the purpose of clarity.

The quaternion Euler parameters are not independent and must satisfy the unit norm condition:

$$\boldsymbol{\theta_q}^{\boldsymbol{i}^T} \boldsymbol{\theta_q}^{\boldsymbol{i}} = 1. \tag{8}$$

The set of equations shown above are solved in Matlab Simulink using the Runge-Kutta solver ode4.

A. Aerodynamics model

Conventional first order linear stability derivatives are used for the aircraft aerodynamics model, namely

$$\begin{gathered} C_L = C_{L_0} + C_{L_\alpha}\alpha + C_{L_{\dot\alpha}} \tfrac{c}{2V}\dot\alpha + C_{L_{\delta_e}}\delta_e, \quad C_D = C_{D_0} + C_{D_\alpha}\alpha, \quad C_Y = C_{Y_\beta}\beta + C_{Y_{\delta_r}}\delta_r, \\ C_l = C_{l_\beta}\beta + C_{l_p}\tfrac{b}{2V}p + C_{l_r}\tfrac{b}{2V}r + C_{l_{\delta_a}}\delta_a + C_{l_{\delta_r}}\delta_r, \\ C_m = C_{m_\alpha}\alpha + C_{m_{\dot\alpha}}\tfrac{c}{2V}\dot\alpha + C_{m_q}\tfrac{c}{2V}q + C_{m_{\delta_e}}\delta_e, \\ C_n = C_{n_\beta}\beta + C_{n_p}\tfrac{b}{2V}p + C_{n_r}\tfrac{b}{2V}r + C_{n_{\delta_a}}\delta_a + C_{n_{\delta_r}}\delta_r, \\ L = \tfrac{1}{2}\rho V^2 S C_L, \quad D = \tfrac{1}{2}\rho V^2 S C_D, \quad Y = \tfrac{1}{2}\rho V^2 S C_Y, \\ l = \tfrac{1}{2}\rho V^2 S b C_l, \quad m = \tfrac{1}{2}\rho V^2 S c C_m, \quad n = \tfrac{1}{2}\rho V^2 S b C_n. \end{gathered} \tag{9}$$

The model and the constant values of the derivatives used are taken from an A-4D fighter aircraft at sea level and Mach 0.4 [14]. A 6.31% scale model is used in the simulation to match the wing span of an approximate subscale BAE Systems Hawk aircraft model, previously tested on the 5-DOF maneuver rig [4]. The reference dimensions, mass and inertia can be seen in appendix B.

The aerodynamic loads (transformed into the inertial axes), along with weight, are inserted as external loads into $\boldsymbol{Q_E}$ in Eq. (1). In addition, the aerodynamics model used is purely to assess the influence of the control technique on the model response and the controller has no knowledge of it.

B. Spherical constraint

In this section C_q and $\boldsymbol{Q_C}$ in Eq. (1) are derived for a spherical constraint by differentiating the equation describing the constraint twice with respect to time. In the case of the spherical constraint, the equation is

$$\sqrt{(x+r)^2 + y^2 + z^2} = r, \tag{10}$$

where r is the radius of the sphere, as shown in figure 4. Note: the origin of the inertial axis is placed at the initial position of the aircraft's center of gravity, at the forward most point on the sphere. Differentiating Eq. (10) twice with respect to time results in

$$\begin{bmatrix} (x+r) & y & z & 0 & 0 & 0 & 0 \end{bmatrix} \begin{bmatrix} \ddot{\boldsymbol{R}} \\ \ddot{\boldsymbol{\theta}}_{\boldsymbol{q}} \end{bmatrix} = -\dot{x}^2 - \dot{y}^2 - \dot{z}^2. \tag{11}$$

Therefore, including the quaternion unit norm condition (differentiating Eq. (8) twice with respect to time), the C_q Jacobian matrix and $\boldsymbol{Q_C}$ vector for the spherical constraint are

$$C_q = \begin{bmatrix} (x-r) & y & z & 0 & 0 & 0 & 0 \\ 0 & 0 & 0 & \theta_0 & \theta_1 & \theta_2 & \theta_3 \end{bmatrix}, \tag{12}$$

$$\boldsymbol{Q_C} = \begin{bmatrix} -\dot{x}^2 - \dot{y}^2 - \dot{z}^2 \\ -\dot{\theta_0}^2 - \dot{\theta_1}^2 - \dot{\theta_2}^2 - \dot{\theta_3}^2 \end{bmatrix}. \tag{13}$$

C. Planar constraint

The planar constraint can be thought of as a special case of the spherical constraint where the sphere radius is infinite. The constraint equations can be derived using a spherical coordinate system, as shown in figure 5. Note: the origin of the inertial axis is again placed at the initial position of the aircraft's center of gravity, at the front of the sphere. The Cartesian coordinates in terms of the inclination (θ) and azimuth (ϕ) angles are

$$x = r \sin\theta_s \cos\phi_s - r, \tag{14}$$

$$y = r \sin\theta_s \sin\phi_s, \tag{15}$$

$$z = r \cos\theta_s. \tag{16}$$

For an arbitrary y and z coordinate, the x coordinate on the sphere in terms of y and z is

$$x = r\sin\left[\arccos\left(\frac{z}{r}\right)\right]\cos\left[\arcsin\left(\frac{y}{r\sin\left[\arccos\left(\frac{z}{r}\right)\right]}\right)\right] - r, \tag{17}$$

since

$$\lim_{r\to\infty}\sin\left[\arccos\left(\frac{z}{r}\right)\right] = 1, \tag{18}$$

$$\lim_{r\to\infty}\cos\left[\arcsin\left(\frac{y}{r}\right)\right] = 1. \tag{19}$$

Therefore, we can write

$$\lim_{r\to\infty} x = 0, \tag{20}$$

and so the expression describing the planar constraint is:

$$x = 0. \tag{21}$$

Similar to the spherical constraint derivation, Eq. (21) is differentiated twice with respect to time to give

$$\begin{bmatrix} 1 & 0 & 0 & 0 & 0 & 0 & 0 \end{bmatrix}\begin{bmatrix} \ddot{\boldsymbol{R}} \\ \ddot{\boldsymbol{\theta}}_{\boldsymbol{q}} \end{bmatrix} = 0. \tag{22}$$

Hence, the C_q Jacobian matrix and $\boldsymbol{Q_C}$ vector (in Eq. (1)) for the planar constraint including the quaternion unit norm condition (differentiating Eq. (8) twice with respect to time) are

$$C_q = \begin{bmatrix} 1 & 0 & 0 & 0 & 0 & 0 & 0 \\ 0 & 0 & 0 & \theta_0 & \theta_1 & \theta_2 & \theta_3 \end{bmatrix}, \tag{23}$$

$$\boldsymbol{Q_C} = \begin{bmatrix} 0 \\ -\dot{\theta_0}^2 - \dot{\theta_1}^2 - \dot{\theta_2}^2 - \dot{\theta_3}^2 \end{bmatrix}. \tag{24}$$

IV. Constrained response comparison

This section compares the longitudinal and lateral-directional mode responses between the unconstrained and constrained aircraft. Here we assumed the inertia of the experimental rig is compensated for ideally, and hence will have no effect on the aircraft's motion. The simulation will consider purely the kinematic constraint, without inertial or aerodynamic effects of the rig itself. The two longitudinal modes for a

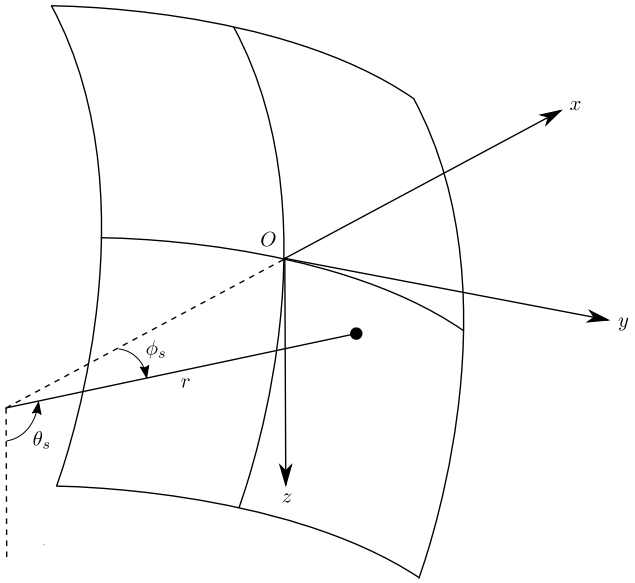

Fig. 5: Spherical coordinates.

conventional aircraft are the short-period and phugoid modes, and the three lateral-directional modes are the Dutch roll, spiral, and roll subsidence modes. All comparisons are made with constant aircraft thrust (including for the constrained aircraft as discussed in the introduction to allow assessment of the effects of the constraint alone) and, to reflect typical wind tunnel dynamic test conditions, an onset velocity of $30m/s$. Constrained aircraft without thrust (similar to conventional models) will be studied in section V. Control surface inputs to excite each mode individually were used [15]. Here, the responses of the short period and phugoid modes, Dutch roll mode, spiral mode, and roll subsidence mode are discussed. For each mode, four types of constraint are considered:

1. Spherical constraint with radius $0.8m$ where the aircraft is constrained to move alone the surface of a sphere
2. Planar constraint where the aircraft only can move along a vertical plane
3. Position fixed constraint where the aircraft center of gravity is fixed and it is only free to rotate
4. Fully unconstrained aircraft in free-flight with constant thrust

As previously shown, the planar constraint is equivalent to the spherical constraint with an infinite radius. Since the aircraft motion is limited to only the yz plane, the aircraft can be thought of as flying at constant ground speed.

The short-period mode which has negligible effect on the forward velocity of the aircraft is a damped oscillation in pitch initiated by a disturbance to the pitch equilibrium [15]. The phugoid mode is a lightly

damped oscillation in aircraft forward speed, pitch, and heave [15]. Figure 6 shows the response for the longitudinal short period and phugoid modes. For this simulation, the disturbance is created by an impulse to the elevator. The aircraft states relevant to each mode are shown as time histories as well as 3D trajectory plots for the unconstrained, $0.8m$ spherical constrained, and planar constrained responses [16]. Specifically the time histories of the aircraft pitch rate (q), angle of attack (α), and heave (z) are shown. Here, the aircraft rotation angles in the trajectory plots have been magnified for clearer visualization as the rotation perturbations are of small magnitude. As expected, the unconstrained aircraft exhibits both the short period and phugiod modes. The phugoid response essentially cannot be observed in any of the constrained responses. Its absence is due to the constraints restricting the aircraft velocity changes required for the phugoid mode to be observed. Therefore, only the short period mode is compared. The apparent oscillatory motion seen in the heave time history is the aircraft moving around the spherical constraint. Comparing the constrained motions, the planar constrained response matches closest with the unconstrained aircraft, followed by the spherical constrained response where the match improves as the arm radius increases (not shown, for brevity). Lastly the fixed position model response shows the largest difference due to the effect the lack of heave motion has on the angle of attack. Although it is not possible to simulate the full phugoid mode while physically constrained, its onset can still be captured if the heave motion is available, after which the effects on the response will be dominated by the velocity limitation the constraint places on the aircraft model.

The Dutch roll mode is a damped oscillation in yaw coupled with roll [15]. Figure 7 shows the response for the Dutch roll mode when excited by a doublet input to the rudder. The time histories of the aircraft yaw rate (r), roll rate (p), angle of attack (α), and angle of sideslip (β) are shown. Apart from the yaw rate of the position fixed response, all constrained motions match the unconstrained motion well. Although the differences when comparing the constrained responses are small, the planar constrained response still gives the best match with the unconstrained aircraft, followed by the spherical constraint and position fixed constraint. Similarly to the short-period mode, the match of the spherically constrained aircraft improves as the sphere radius increases (not shown).

The spiral mode is a nonoscillatory mode involving coupled motion in roll, yaw, and sideslip [15]. The stability of the long term motion is determined by the dihedral effect and the fin effect. The motion is stable if the dihedral effect is greater or unstable if the fin effect is greater [15]. For the A-4D aircraft used in this simulation the spiral mode is stable. Figure 8 shows the response for the spiral mode onset which is excited by a step input to the rudder. The time histories of the aircraft roll angle (ϕ), angle of attack (α), angle of sideslip (β), total velocity (V), and heave (z) are shown. It is unlikely that the response beyond the *onset* of the spiral mode can be physically simulated while constrained due to the size of the motions involved.

Similarly to the Dutch roll mode, apart from the fixed position response, the constrained responses match the unconstrained well up to 2.75 seconds, after which the velocity restrictions produced by the constraints dominate the response. When inspected closer, again the planar constrained response gives the best match with the unconstrained aircraft, followed by the spherical constrained response where a larger radius gives a better match. The position fixed response is an oddity as its response, beyond 2.75 seconds, seems to match the unconstrained aircraft better than the spherical constrained response for angle of attack, sideslip and total velocity. The larger difference past 2.75 seconds for the spherical constraint is essentially due to the constraint's restriction in velocity variation impacting the overall spiral motion. The velocity restriction causes the motion to deviate from its natural response as a result.

The roll subsidence mode is also a nonoscillatory mode, consisting of pure roll [15]. Figure 9 shows the response for the roll subsidence mode, excited by applying a square pulse to the aileron. The time histories of the aircraft roll rate (p), roll angle (ϕ), angle of attack (α), and angle of sideslip (β) are shown. Since the lateral response of this mode is rapid, the effects of the physical constraints become apparent past 3 seconds. The effect can be seen for the spherical constrained response where again the restrictions to aircraft velocity exacerbate the lateral motion causing the aircraft to circle around the constraint. Prior to 3 seconds, the constrained responses match well with the unconstrained as there is very little lateral motion. The better match is a result of the very similar velocity variations between the constrained and unconstrained cases up to this point in time. Again, the position fixed response shows the most significant difference as there is no lateral motion.

With regards to motion accuracy in this analysis in general the best match to the unconstrained aircraft is the planar constrained motion, followed by the spherically constrained aircraft and the position fixed response having the largest difference. In addition we observed modes which require a large change to the aircraft velocity vector such as the phugiod mode cannot be physically simulated while constrained. Although the responses for a range of spherical constraint radii are not presented in this study, the spherically constrained aircraft motion converged to the planar constrained response as the spherical constraint radius increases. Reducing this radius further increases the discrepancy in motion. The position fixed constraint further limits the aircraft motion to rotation only with no translation. Note: the comparisons presented here assume the constrained aircraft is capable of producing thrust, so revealing the effect of the constraint alone. In section V a constrained aircraft without thrust is simulated – as would be the case in conventional testing – where the lack of thrust is shown to exacerbate the effect of the kinematic constraint.

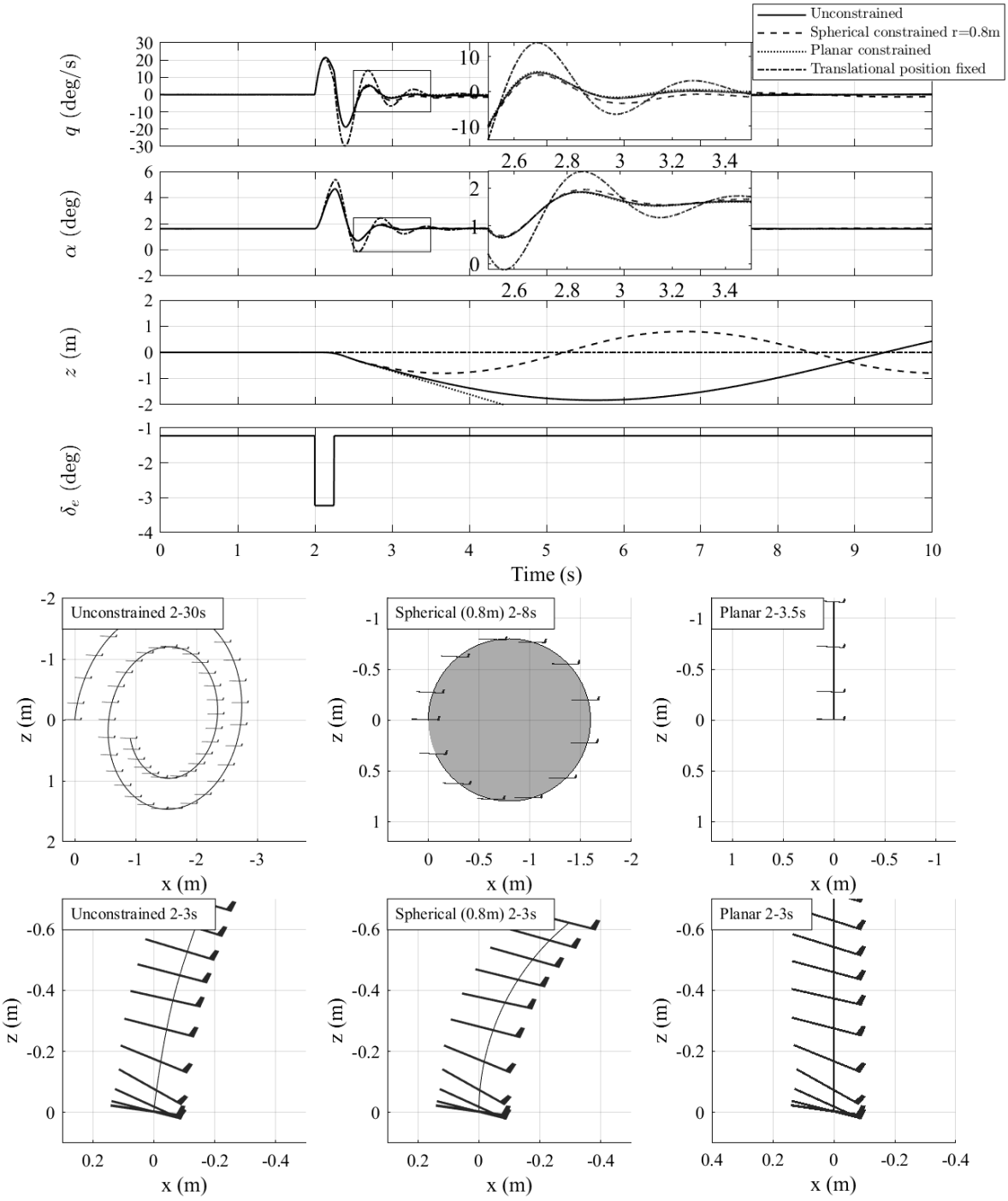

Fig. 6: Short-period and phugoid mode responses.

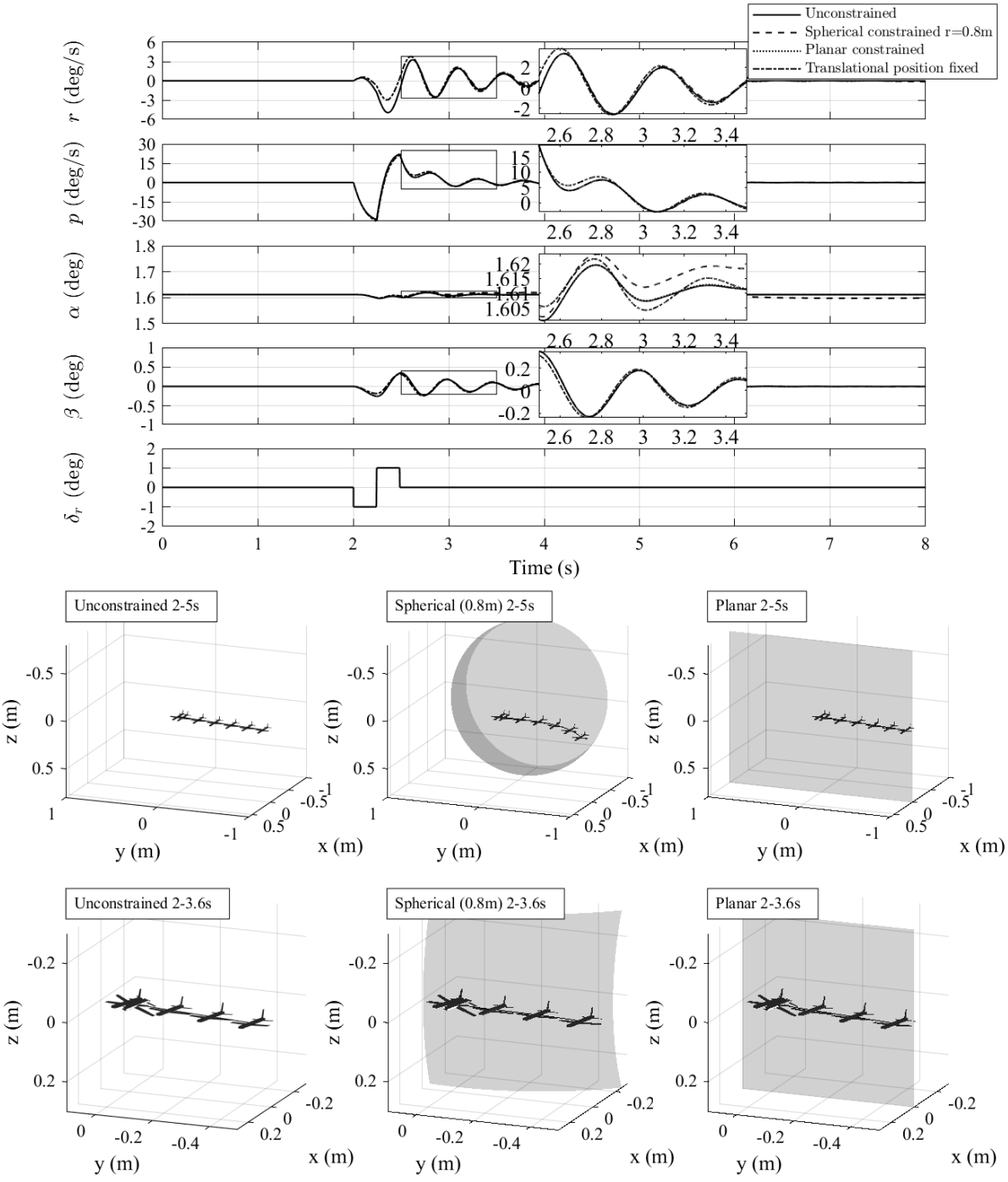

Fig. 7: Dutch roll mode responses.

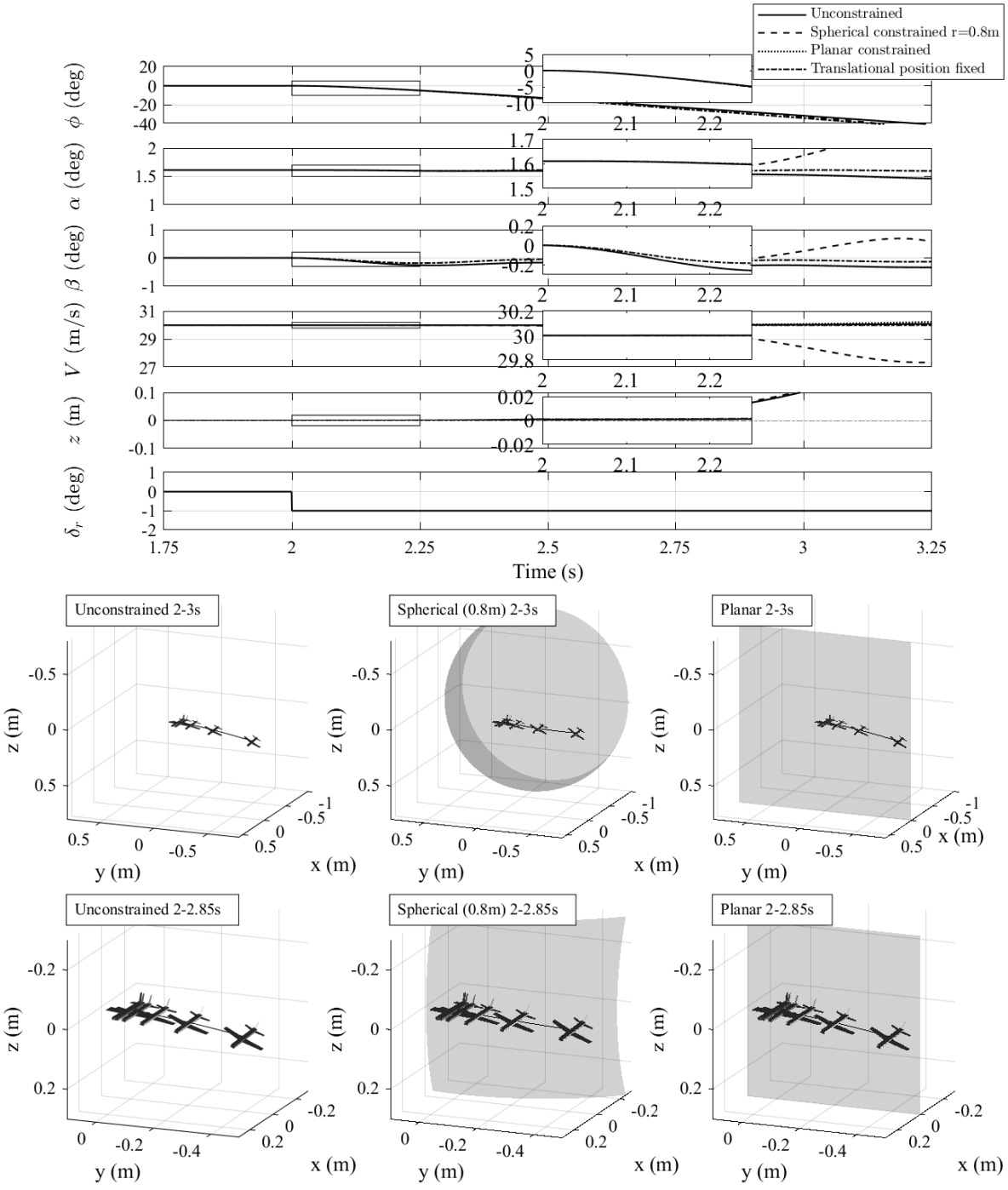

Fig. 8: Spiral mode responses.

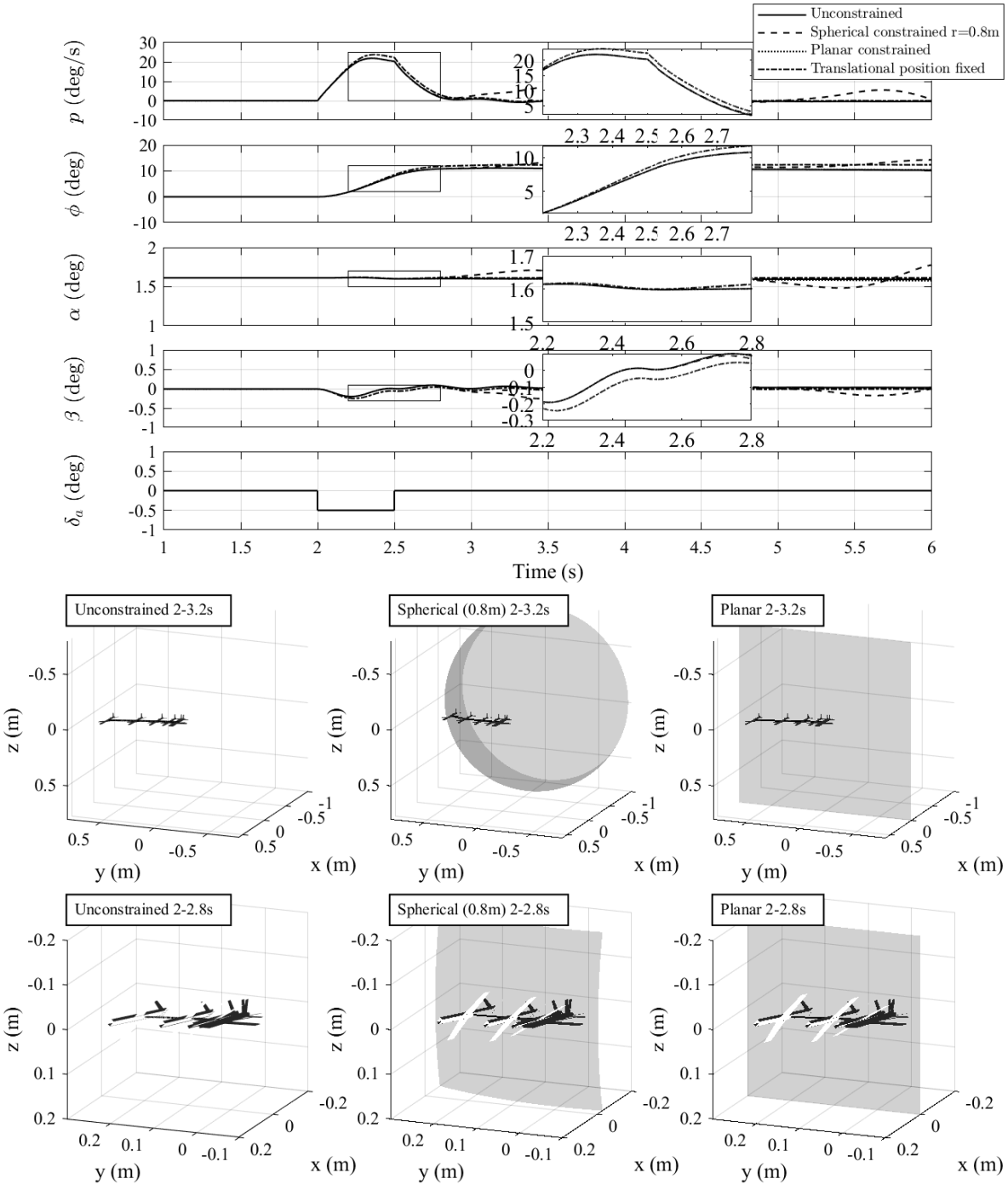

Fig. 9: Roll subsidence mode responses.

V. Kinematic constraint compensation

An ideal planar constraint will provide a longitudinal force through the yz plane to ensure the aircraft has a fixed position in the wind tunnel x direction (or constant ground speed in flight) with zero vertical or lateral forces which is equivalent to ensuring the inertial forces of the rig are fully compensated. In the previous section we assumed this compensation, via an inverse model of the rig, for all the rig configurations. However for a spherically constrained aircraft the optimum applied forces to mimic free flight as close as possible are more complicated, as discussed here.

In this section we propose a technique to improve the response of a spherically constrained aircraft to better match a planar constrained aircraft (and thus, as shown in section IV, a better match with a free-flying aircraft). An experimental rig having a spherical constraint such as the maneuver rig shown in figure 1 has the ability to apply an external tangential force on the aircraft model using its aerodynamic compensator ($\mathbf{F_c}$, as shown in figure 10). Analyzing the planar constraint one can see any aerodynamic or inertial force in the x direction (figure 4(b)) is matched by the constraint and does not affect the aircraft's motion in the yz plane. However, analyzing the spherical constraint, aerodynamic and inertial forces in the x direction create moments about the center of the sphere once there is any heave or sway motion to create a moment arm. These forces are used to derive the external tangential force ($\mathbf{F_c}$) to negate this moment. The kinematic compensation concept proposed here is to introduce rig compensator feedback control to impose the required tangential force on the aircraft model. This scheme requires load cell measurement of the reaction forces between the experimental rig and the mounted aircraft model. Here the constrained aircraft does not produce thrust, as is the case in almost all wind tunnel testing.

A. Derivation of $\mathbf{F_c}$

Here we derive the external tangential force ($\mathbf{F_c}$) which will be applied to the aircraft model to compensate for the effects of the spherical constraint in order to match a constant ground speed aircraft. The derivation is achieved by canceling the moment created by resultant aerodynamic and inertial force (X_{in}) in the x direction indicated in figure 4. Note: X_{in} includes aerodynamic, inertial and propulsive forces of the aircraft model. If the aircraft model creates thrust then the magnitude of X_{in} is small, however if thrust is not present then X_{in} is large and dominated by drag. Therefore, $\mathbf{F_c}$ is the negative of the tangential component

of X_{in}:

$$\mathbf{F_c} = -\mathbf{X_{tan}}, \tag{25}$$

$$\mathbf{X_{tan}} = X_{in}\begin{pmatrix}1\\0\\0\end{pmatrix} - X_{in_{rad}}\hat{\mathbf{p}}, \tag{26}$$

where $X_{in_{rad}}$ is the radial component of X_{in} and $\hat{\mathbf{p}}$ is the normalized position vector of the aircraft relative to the center of the sphere with respect to the inertial axis system. Figure 10 shows a diagram depicting these forces, where the forces in boxes are matched by the spherical constraint reaction force, which can be measured using a load cell. Note: all radial components are positive in the outward direction. X_{in} and $X_{in_{rad}}$ can be calculated by

$$X_{in} = {}^{X_{in_{rad}}}\Big/_{\left[\begin{pmatrix}1\\0\\0\end{pmatrix}\cdot\hat{\mathbf{p}}\right]}, \tag{27}$$

$$X_{in_{rad}} = -\left\{R_{rad}\hat{\mathbf{p}} + \left[\left(Y_{in}\begin{pmatrix}0\\1\\0\end{pmatrix} + Z_{in}\begin{pmatrix}0\\0\\1\end{pmatrix}\right)\cdot\hat{\mathbf{p}}\right]\hat{\mathbf{p}} - m\mathbf{a_{cen}}\right\}\cdot\hat{\mathbf{p}}, \tag{28}$$

where R_{rad} is the radial reaction force measured by the load cell. In the ideal case the tangential reaction force will be zero if the inertia of the experimental rig is fully compensated. Y_{in} and Z_{in} are the resultant aerodynamic and inertial forces in the y and z directions respectively. m is the mass of the model aircraft and $\mathbf{a_{cen}}$ is the centripetal acceleration:

$$\mathbf{a_{cen}} = -r\omega^2\hat{\mathbf{p}}, \tag{29}$$

where r is the sphere radius and ω is the angular velocity of the aircraft about the sphere. Y_{in} and Z_{in} can be found by first calculating the projected total aerodynamic and inertial force onto the yz plane:

$$\mathbf{F_{yz}} = \frac{\|\mathbf{F_{tan}}\|}{\hat{\mathbf{v}}_\mathbf{p} \cdot \hat{\mathbf{F}}_\mathbf{tan}} \hat{\mathbf{v}}_\mathbf{p}, \tag{30}$$

$$\hat{\mathbf{v}}_\mathbf{p} = (\hat{\mathbf{p}} \times \mathbf{F_{tan}}) \times \begin{pmatrix} 1 \\ 0 \\ 0 \end{pmatrix}, \tag{31}$$

where $\hat{\mathbf{v}}_\mathbf{p}$ is a vector in line with the yz plane and $\mathbf{F_{tan}}$, and $\mathbf{F_{tan}}$ is

$$\mathbf{F_{tan}} = m\mathbf{a_{tan}} \text{ with: } \mathbf{a_{tan}} = \mathbf{a} - \mathbf{a_{cen}}. \tag{32}$$

Here $\mathbf{a}$ is the total acceleration vector of the aircraft in the inertial axes. Finally Y_{in} and Z_{in} can be expressed as

$$Y_{in} = \mathbf{F_{yz}} \cdot \begin{pmatrix} 0 \\ 1 \\ 0 \end{pmatrix}, \; Z_{in} = \mathbf{F_{yz}} \cdot \begin{pmatrix} 0 \\ 0 \\ 1 \end{pmatrix}. \tag{33}$$

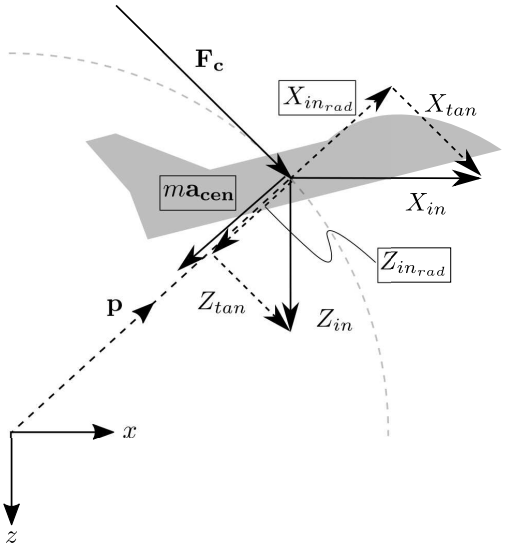

Fig. 10: Spherical constraint forces.

B. Response comparisons with F_c

This section presents the effects on the aircraft response when the external tangential force $\mathbf{F_c}$ is applied to the model through the rig. The aircraft response on a spherical constraint with radius $0.8m$ is compared with the response of a planar constrained and unconstrained aircraft, both with and without $\mathbf{F_c}$. In the case where $\mathbf{F_c}$ is not used we assume perfect compensation for the inertial forces of the rig as in the previous section. In the following simulations all constrained aircraft are assumed to have no thrust producing capability, as in most wind tunnel aircraft models, except the unconstrained aircraft maintains a constant thrust which would have to be provided by the model. The lack of thrust in the constrained aircraft setup exacerbates the effect of the total aerodynamic force in the X direction making the aircraft unstable while spherically constrained. The lack of thrust results in an increase in magnitude of X_{in} due to drag, akin to an inverted pendulum.

The responses are compared to the unconstrained response qualitatively using time history plots as well as quantitatively using root mean square errors. Additionally, the known aerodynamic coefficients are estimated from the responses: this is often the purpose of dynamic testing and free-flight tests, and is used here as a means of evaluating the magnitude of the constraint effects on the aircraft model motions – and as a measure of the extent to which the application of $\mathbf{F_c}$ improves them. The coefficients are estimated using the equation error method parameter estimation technique. [17] For each mode comparison only one key variable is presented. The control surface input used is the exact same as was used in section IV. Further details are given later in this section.

Figure 11 shows the comparison graph for pitch rate q of the short-period mode and the root mean square errors are shown in Table 1. The spherically constrained response with $\mathbf{F_c}$ can be observed to initially follow the response without $\mathbf{F_c}$, however the divergent behavior present without $\mathbf{F_c}$ is suppressed when $\mathbf{F_c}$ is introduced, improving its match with the free-flight unconstrained or planar constrained responses. The root mean square error is calculated for the range two and four seconds. Significant reduction in error, of up to 80%, can be obtained using $\mathbf{F_c}$.

Figure 12 shows the comparison for yaw rate r of the Dutch roll mode and the root mean square errors are shown in Table 2. Similar to the short-period response, $\mathbf{F_c}$ prevents the response from diverging, giving

Table 1: Short-period mode: root mean square error relative to unconstrained responses (2 to 4 seconds)

States	**RMS without F_c**	**RMS with F_c**	**% change**
q (deg/s)	3.59	0.731	-79.6 %
α (deg)	0.166	0.0482	-70.9 %
z (m)	0.373	0.238	-36.3 %

Table 2: Dutch roll mode: root mean square error relative to unconstrained responses (2 to 4.5 seconds)

States	RMS without F_c	RMS with F_c	% change
r (deg/s)	1.93	0.168	-91.3%
p (deg/s)	1.33	0.0915	-93.1%
β (deg)	0.0524	0.00500	-90.5%

a closer match with the planar and unconstrained responses. The root mean square error also indicates a significant improvement.

Applying $\mathbf{F_c}$ to the spiral mode and roll subsidence mode showed little to no improvement, and so are not presented here for brevity. The spiral mode involves large translational motion and therefore is normally difficult to simulate while constrained on a rig within the confines of a wind tunnel, although its onset may still be captured. No improvement was seen when $\mathbf{F_c}$ was applied to the roll subsidence mode since the motion does not involve significant translation. However this outcome is dependent on the configuration of the aircraft being tested. An aircraft model with perhaps a larger vertical tail than the model being simulated here could have induced significant lateral translation when rolling, a feature which is likely to be captured better with the use of $\mathbf{F_c}$.

Out of all the constraints, the planar constraint responses give the best match with the unconstrained aircraft. The remaining difference in the spherical constraint response is due to the imposed restriction on the aircraft's velocity vector as the aircraft is forced to move along the surface of a sphere. In turn, this restriction affects the aerodynamic forces and moments, which then again affect its motion. Although applying the external tangential force $\mathbf{F_c}$ does not give an exact match, it is possible to improve the aircraft's response to better match the planar constrained or unconstrained aircraft.

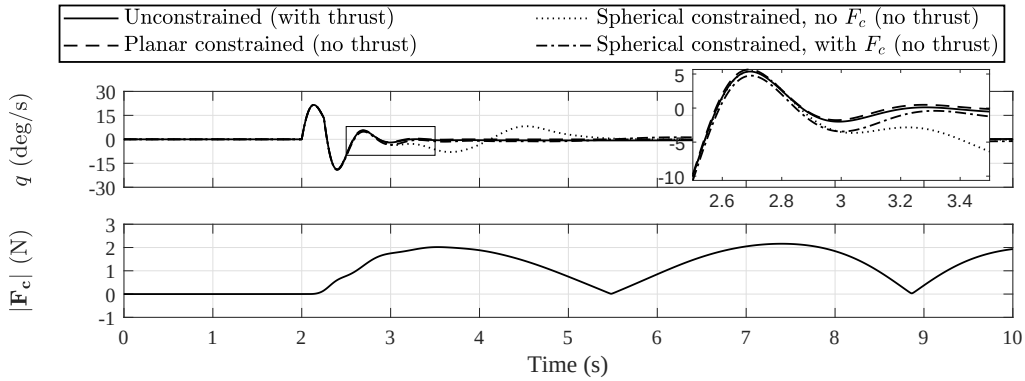

Fig. 11: Short-period mode responses with and without F_c.

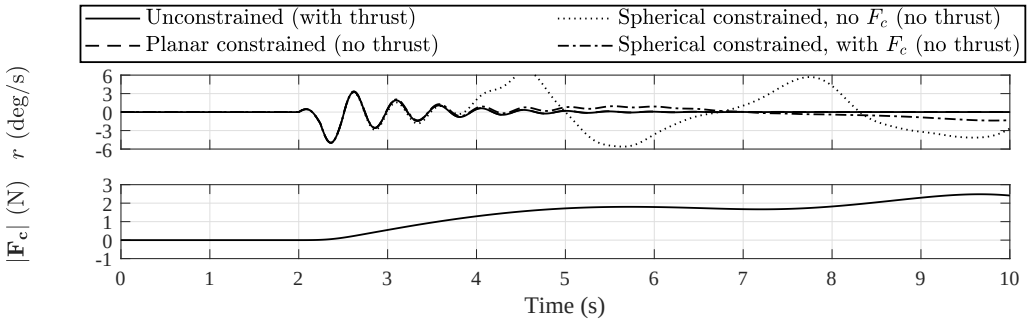

Fig. 12: Dutch roll mode responses with and without F_c.

As mentioned above, in addition to the use of the root mean square error to quantitatively measure the improvement due to $\mathbf{F_c}$ evaluation of the aerodynamic coefficients using parameter estimation from the aircraft model's motion response is also used. Even though conventionally these coefficients are measured using static and forced dynamic tests using a load cell within a wind tunnel, the coefficients are estimated here using the aircraft motion responses instead, within the same environment. The aim is to provide a means of measuring the effects of the kinematic constraints on motion-derived coefficients and assess how $\mathbf{F_c}$ can improve the accuracy of the observed motion. The equation error method was chosen to estimate the aerodynamic parameters and its effectiveness is demonstrated by re-identifying the known aerodynamic coefficients from the motion of the unconstrained aircraft model [17].

The mathematical model for the aircraft used for the estimation assumes it is in free-flight, and all its mass and inertial properties are known. As an example, the system of equations to be solved for the short-period mode case is:

$$\begin{bmatrix} 1 & \alpha & \frac{c}{2V}\dot{\alpha} & \delta_e \\ \vdots & \vdots & \vdots & \vdots \\ 1 & \alpha_n & \frac{c}{2V_n}\dot{\alpha}_n & \delta_{e_n} \end{bmatrix} \begin{bmatrix} C_{L_0} \\ C_{L_\alpha} \\ C_{L_{\dot{\alpha}}} \\ C_{L_{\delta_e}} \end{bmatrix} = \begin{bmatrix} C_L \\ \vdots \\ C_{L_n} \end{bmatrix} \tag{34}$$

This solution is essentially a least-squares estimation where the right hand side of the equation needs to be multiplied with the pseudo-inverse of the first left hand side matrix to solve for the unknown vector of aerodynamic parameters. The subscript n represents the total number of measurements taken within the time period. The total lift coefficient (C_L) is calculated using the measured acceleration together with the aircraft's mass and Eq. (9).

For conventional parameter estimation, specific control surface inputs such as a 3-2-1-1 signal are used to produce sufficient excitation to all states of the aircraft. For this investigation, a Morlet wavelet control surface input having a central frequency equal to the natural frequency of each oscillatory mode is used. The aircraft states are more effectively excited with this input than those applied in section VI and allows the effectiveness of the compensation technique to be determined. The natural frequency of each mode was found using a Fast Fourier Transform of its responses. The short-period and Dutch roll modes for the model aircraft have frequencies of 1.67 Hz and 2.00 Hz respectively. Tables 3 and 4 show the estimated parameters for these two oscillatory modes and their corresponding responses are shown in figure 13 and figure 14. The parameters for the free-flying case are estimated first, to demonstrate the accuracy of the estimation technique. The free-flying coefficients were estimated to within 1% error showing the suitability of the estimation technique and input used.

Comparing all coefficients for each mode, in general $\mathbf{F_c}$ improves coefficients related to translational motion, such as C_L and C_Y. The estimation of all moment coefficients are accurate even without $\mathbf{F_c}$ provided the excitation of the given state is large enough. Applying $\mathbf{F_c}$ shows negligible change to these estimated moment coefficients which is not unexpected as the kinematic constraints affect aircraft model translations rather than its rotations.

The short-period mode parameter estimation results are shown in table 3. The estimation of all C_L coefficients show improvement when $\mathbf{F_c}$ is introduced. Although $\mathbf{F_c}$ does improve the estimation errors, reducing them to the same order as the planar values, the error is still significant. $C_{L_{\dot{\alpha}}}$ is estimated poorly for all constrained responses since the magnitude of $\dot{\alpha}$ is small relative to the aircraft's other states and has a very small contribution to the total lift coefficient. Also the drag is not estimated accurately regardless of whether $\mathbf{F_c}$ is used or not because the kinematic constraint limits the aircraft's acceleration due to drag creating a considerable error on the estimated drag force.

The Dutch roll parameter estimation results are shown in table 4. Similar to the short-period case, $\mathbf{F_c}$ improves the estimation of the side force (C_Y) derivatives matching the error of the planar constrained values.

Here, the aerodynamic coefficients directly related to the heave and sway motions of the aircraft (C_L and C_Y derivatives) are improved with the use of the external force $\mathbf{F_c}$ provided the control surface input sufficiently excites the aircraft states. Aerodynamic coefficient estimation for the roll subsidence and spiral modes show the same trend but are omitted in the interests of brevity.

VI. Effect of delayed $\mathbf{F_c}$ signal

The study thus far has assumed there are no delays when applying the external compensating force $\mathbf{F_c}$. When considering a practical implementation of this technique, delays are inevitable. For example, sources of such delays reported for the 5-DOF maneuver rig [4, 9] include wireless signal transmission delays and aerodynamic compensator control surface actuation lag, which were estimated to be about 4 and 100 milliseconds respectively. Here, we investigate the influence of delay by running short-period mode simulations with delays ranging from 0 to 250 milliseconds. The effect on the Dutch roll mode follows the same trend although with less degradation in motion accuracy. Figure 15 shows the simplified block diagram of the mathematical simulation including the introduced delay. Here, all control surface actuation is assumed to be ideal and so no feedback control is used within the aircraft model.

Figure 16 shows a comparison of the short-period mode responses with a range of communication delays. Major differences are observed in the heave responses and the match with the free-flying aircraft deteriorates as the delay increases. Table 5 shows the quantitative comparison between the responses using the root mean

Table 3: Estimating aerodynamic coefficients from short-period response (0 to 6 seconds)

Aerodynamic coefficients	Simulation model value	Unconstrained (with thrust)		Planar (no thrust)		Spherical without $\mathbf{F_c}$ 0.8 m (no thrust)		Spherical with $\mathbf{F_c}$ 0.8 m (no thrust)	
		Estimate	% error	Estimate	% error	Estimate	% error	Estimate	% error
C_{L_0}	0.28	0.28	0.0%	0.28	0.0%	0.28	**0.7%**	0.28	**0.0%**
C_{L_α}	3.5	3.5	0.0%	3.5	0.0%	3.4	**-1.5%**	3.4	**-0.3%**
$C_{L_{\dot{\alpha}}}$	0.72	0.73	0.8%	1.0	44.4%	2.1	**185.0%**	0.91	**26.9%**
$C_{L_{\delta_e}}$	0.36	0.36	0.0%	0.36	0.0%	0.43	**18.1%**	0.36	**-0.8%**
C_{D_0}	0.030	0.030	0.0%	-0.00016	-101.0%	-0.00079	-97.4%	-0.00027	-101.0%
C_{D_α}	0.30	0.30	0.0%	0.0053	-98.2%	-0.012	-104.0%	0.0093	-96.9%
C_{M_α}	-0.38	-0.38	0.3%	-0.38	0.0%	-0.38	0.3%	-0.38	0.0%
$C_{M_{\dot{\alpha}}}$	-1.1	-1.1	0.0%	-1.1	0.0%	-1.1	0.0%	-1.1	0.0%
C_{M_q}	-3.6	-3.6	0.0%	-3.6	0.0%	-3.6	0.0%	-3.6	0.0%
$C_{M_{\delta_e}}$	-0.50	-0.50	0.2%	-0.50	0.2%	-0.50	0.2%	-0.50	0.2%

Table 4: Estimating aerodynamic coefficients from Dutch roll response (0 to 6 seconds)

Aerodynamic coefficients	Simulation model value	Unconstrained (with thrust)		Planar (no thrust)		Spherical without $\mathbf{F_c}$ 0.8 m (no thrust)		Spherical with $\mathbf{F_c}$ 0.8 m (no thrust)	
		Estimate	% error	Estimate	% error	Estimate	% error	Estimate	% error
C_{Y_β}	-0.98	-0.98	0.0%	-0.98	-0.1%	-0.98	**-0.5%**	-0.98	**-0.1%**
$C_{Y_{\delta_r}}$	0.17	0.17	0.0%	0.17	0.0%	0.17	**1.8%**	0.17	**0.0%**
C_{l_β}	-0.12	-0.13	5.8%	-0.13	5.8%	-0.13	5.8%	-0.13	5.8%
C_{l_p}	-0.26	-0.26	0.0%	-0.26	0.0%	-0.26	0.0%	-0.26	0.0%
C_{l_r}	0.14	0.15	7.1%	0.15	7.1%	0.15	7.1%	0.15	7.1%
$C_{l_{\delta_r}}$	0.11	0.11	1.0%	0.11	1.0%	0.11	1.0%	0.11	1.0%
C_{n_β}	0.25	0.25	-1.2%	0.25	-1.2%	0.25	-1.2%	0.25	-1.2%
C_{n_p}	0.020	0.015	-31.4%	0.015	-31.8%	0.015	-31.8%	0.015	-31.8%
C_{n_r}	-0.35	-0.35	-1.4%	-0.35	-1.4%	-0.35	-1.4%	-0.35	-1.4%
$C_{n_{\delta_r}}$	-0.030	-0.029	-9.1%	-0.029	-9.1%	-0.029	-9.1%	-0.029	-9.1%

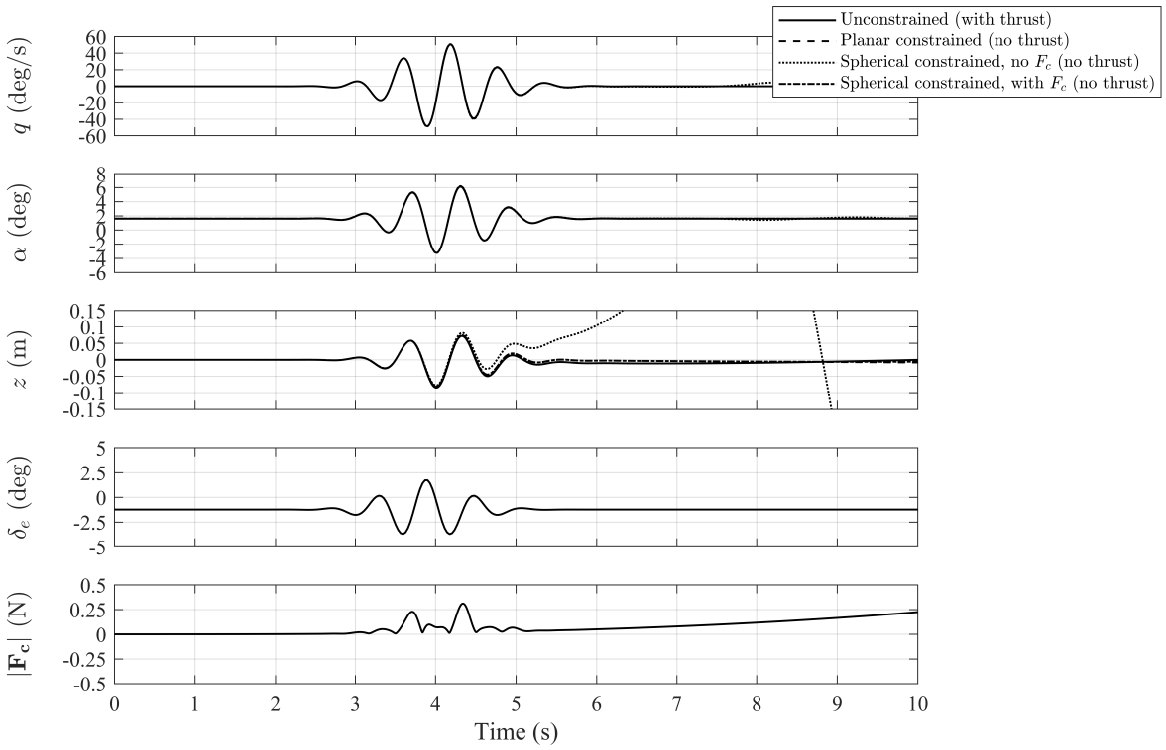

Fig. 13: Short-period mode responses with a Morlet wavelet.

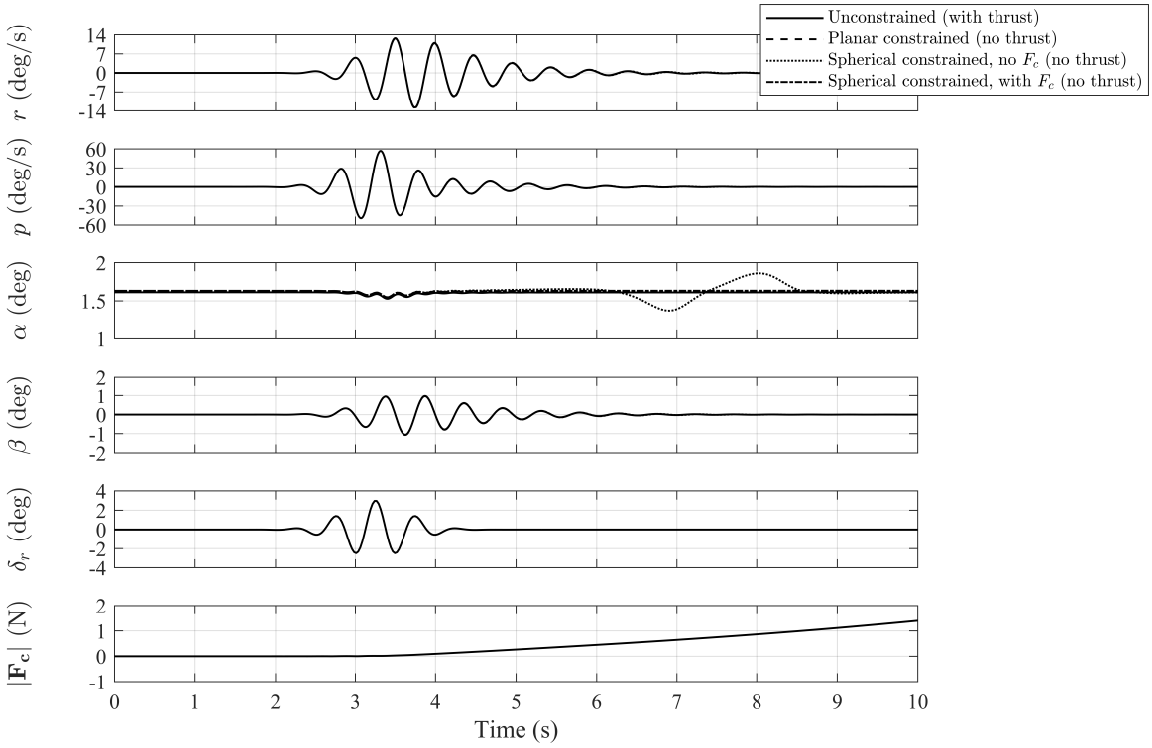

Fig. 14: Dutch roll mode responses with a Morlet wavelet.

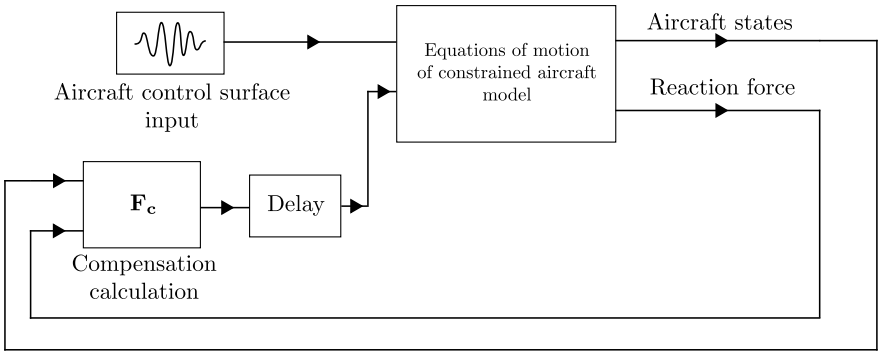

Fig. 15: Simplified block diagram of the simulation.

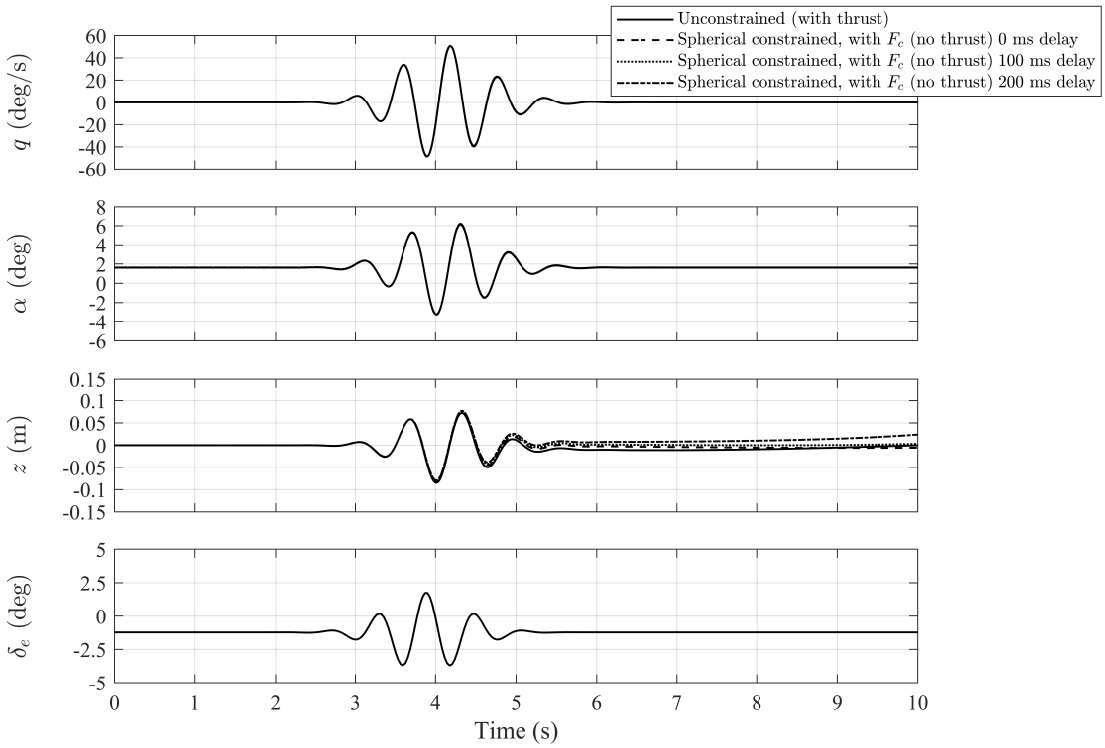

Fig. 16: Short-period response with $\mathbf{F_c}$ compensation including transmission delay.

square error of each state. The match with the unconstrained response decreases as the delay is increased. The last column of the table shows the error when no $\mathbf{F_c}$ compensation is used. These RMS values show the equivalence between having no compensation and having a delay of approximately 150 ms with compensation for the q and α states. Therefore in order to benefit from the compensation technique proposed here, the delay needs to be less than 150 ms. An exception to this is the z state error which is still lower than when $\mathbf{F_c}$ is not used even with a delay of 250 ms.

Table 5: RMS comparison between the spherically constrained aircraft model (without thrust) responses with delayed $\mathbf{F_c}$ relative to the unconstrained response (0 to 6 seconds)

States	0 ms delay	50 ms delay	100 ms delay	150 ms delay	200 ms delay	250 ms delay	No $\mathbf{F_c}$
q (deg/s)	0.116	0.135	0.169	0.202	0.229	0.246	0.198
α (deg)	0.0218	0.0229	0.0247	0.0266	0.0281	0.0289	0.0265
z (m)	0.00344	0.00430	0.00524	0.00628	0.00740	0.00858	0.0312

VII. Conclusion

Various aircraft response modes have been studied under different kinematic constraints with the aircraft model incorporating thrust. The planar constraint, where the aircraft is constrained to move in a plane perpendicular to the oncoming air flow, gave the best response relative to an unconstrained free-flying aircraft, with a spherical constraint response exhibiting a deterioration in terms of motion match relative to the unconstrained aircraft model.

Aircraft motion with substantial heave and sway motions were most susceptible to effects of this kinematic constraint whereas rotational responses were not noticeably affected. The change to the heave and sway responses of the spherically constrained aircraft was largely due to the moment created by drag when thrust is not present, which is the case for most wind tunnel tests. An external force, $\mathbf{F_c}$, was derived in order to compensate for this moment, based on feedback of measured force to cancel the moment created by the resultant aerodynamic and inertial force components. Applying this force showed improvements to heave and sway responses of the aircraft giving a closer, though not perfect, match with a free-flying aircraft. Effects of compensator control delays have also been presented where, although the presence of a delay deteriorates the match with the unconstrained aircraft, compensation remains feasible for practical values of delay.

Acknowledgements

The authors would like to acknowledge Prof. Mikhail Goman from De Montfort University, who devised the concept of the maneuver rig layout. The authors would also like to thank Sergio A. Araujo-Estrada from the University of Bristol and Zheng Gong from Nanjing University of Aeronautics and Astronautics for their valuable support and advice on data acquisition and control development. S. A. Neild would like to acknowledge the support of the EPSRC through fellowship EP/K005375/1. P. D. B. Navaratna would like to thank the University of Bristol for the alumni-funded PhD scholarship.

Appendix A: Quaternion transformation matrices

$$E^i = \begin{bmatrix} -\theta_1{}^i & \theta_0{}^i & -\theta_3{}^i & \theta_2{}^i \\ -\theta_2{}^i & \theta_3{}^i & \theta_0{}^i & -\theta_1{}^i \\ -\theta_3{}^i & -\theta_2{}^i & \theta_1{}^i & \theta_0{}^i \end{bmatrix}, \overline{E}^i = \begin{bmatrix} -\theta_1{}^i & \theta_0{}^i & \theta_3{}^i & -\theta_2{}^i \\ -\theta_2{}^i & -\theta_3{}^i & \theta_0{}^i & \theta_1{}^i \\ -\theta_3{}^i & \theta_2{}^i & -\theta_1{}^i & \theta_0{}^i \end{bmatrix} \tag{35}$$

$$A^i = E^i \overline{E}^{i^T}, G^i = 2E^i, \overline{G}^i = 2\overline{E}^i \tag{36}$$

Appendix B: Subscale aircraft model properties

Table B.1 presents the reference dimensions, mass and inertia of the subscale model aircraft used in the computational simulation: 6.31% scale model of a A-4D aircraft [14].

Table B.1: Model aircraft reference dimensions, mass and inertia properties

Property	**Symbol**	**Value**
Wing area	S	0.0961 m^2
Mean aerodynamic chord	c	0.208 m
Span	b	0.529 m
Mass	m	2.00 kg
Inertia	I_{xx}	0.0109 kg m^2
	I_{yy}	0.0350 kg m^2
	I_{zz}	0.0395 kg m^2
	I_{xy}	0.00 kg m^2
	I_{xz}	0.00180 kg m^2
	I_{yz}	0.00 kg m^2

References

[1] Owens, B., Brandon, J., Croom, M., Fremaux, M., Heim, G., and Vicroy, D., "Overview of Dynamic Test Techniques for Flight Dynamics Research at NASA LaRC," *25th AIAA Aerodynamic Measurement Technology and Ground Testing Conference*, No. AIAA 2006-3146, 2006, doi:10.2514/6.2006-3146.

[2] Muse, J. A., Kutay, A., and Calise, A. J., "Novel force control traverse for simulating UAV flight in wind tunnel," *AIAA Atmospheric Flight Mechanics Conference*, No. AIAA 2008-6714, 2008, doi:10.2514/6.2008-6714.

[3] Lutze, F. H. and Fan, Y., "Unsteady Aerodynamic Testing Using the Dynamic Plunge Pitch and Roll Model Mount," Department of Aerospace and Ocean Engineering, Virginia Polytechnic Institute and State University, NASA Grant NAG-1-1737, 1999, Document ID: 20000013325.

[4] Araujo-Estrada, S. A., Gong, Z., Lowenberg, M. H., Neild, S., and Goman, M., "Wind Tunnel Manoeuvre Rig: A Multi-DOF Test Platform for Model Aircraft," *54th AIAA Aerospace Sciences Meeting*, No. AIAA 2016-2119, 2016, doi:10.2514/6.2016-2119.

[5] Bergmann, A., Huebner, A., and Loeser, T., "Experimental and numerical research on the aerodynamics of unsteady moving aircraft," *Progress in Aerospace Sciences*, Vol. 44, No. 2, 2008, pp. 121–137, doi: 10.1016/j.paerosci.2007.10.006.

[6] Araujo-Estrada, S. A., Lowenberg, M. H., Neild, S., and Goman, M., "Evaluation of Aircraft Model Upset Behaviour Using Wind Tunnel Manoeuvre Rig," *AIAA Atmospheric Flight Mechanics Conference*, No. AIAA 2015-0750, 2015, doi:10.2514/6.2015-0750.

[7] Pattinson, J., Lowenberg, M., and Goman, M., "A multi-degree-of-freedom rig for the wind tunnel determination of dynamic data," *AIAA Atmospheric Flight Mechanics Conference*, No. AIAA 2009-5727, 2009, doi:10.2514/6.2009-5727.

[8] Pattinson, J., Lowenberg, M., and Goman, M., "Characterisation of wind tunnel observed, large-amplitude pitch limit-cycles," *AIAA Atmospheric Flight Mechanics Conference*, No. AIAA 2011-6526, 2011, doi:10.2514/6.2011-6526.

[9] Peyada, N., Ghosh, A., and Go, T., "Mathematical modelling, simulation, and estimation of aircraft parameters using five degree-of-freedom dynamic test rig," *Proceedings of the Institution of Mechanical Engineers, Part G: Journal of Aerospace Engineering*, Vol. 226, No. 1, 2011, pp. 55–63, doi: 10.1177/0954410011407265.

[10] Pattinson, J., Lowenberg, M. H., and Goman, M. G., "Multi-Degree-of-Freedom Wind-Tunnel Maneuver Rig for Dynamic Simulation and Aerodynamic Model Identification," *Journal of Aircraft*, Vol. 50, No. 2, 2013, pp. 551–566, doi:10.2514/1.c031924.

[11] Prosser, D., *Flapping wing design for a dragonfly-like micro air vehicle*, Master's thesis, Rochester Institute of Technology, 2011, Accessed from https://scholarworks.rit.edu/theses/5804.

[12] Navaratna, P. D. B., Lowenberg, M. H., Neild, S., and Zhang, X., "Physical simulation of free-flight in captive wind tunnel tests," *Applied Aerodynamics Conference*, Royal Aeronautical Society, Bristol, 2016.

[13] Shabana, A. A., *Dynamics of Multibody Systems*, Cambridge University Press, ISBN 0-521-85011-8, 3rd ed., 2005, doi:10.1017/CBO9780511610523.

[14] Nelson, R. C., *Flight Stability and Automatic Control*, McGraw-Hill, 1989.

[15] Cook, M., *Flight Dynamics Principles: A Linear Systems Approach to Aircraft Stability and Control*, Elsevier, ISBN 9780080982427, 3rd ed., 2013, doi:10.1016/c2010-0-65889-5.

[16] Scordamaglia, V., "Trajectory and Attitude Plot Version 3 for MATLAB 6.5.1 (R13SP1)," https://uk.mathworks.com/matlabcentral/fileexchange/5656-trajectory-and-attitude-plot-version-3, date accessed: 15-05-2016.

[17] Jategaonkar, R. V., *Flight Vehicle System Identification: A Time-domain Methodology*, Progress in Astronautics and Aeronautics, American Institute of Aeronautics and Astronautics, ISBN 9781563478369, 2006, doi:10.2514/4.102783.